3. Biot–Savart Law in Cosmic Plasma

3.1 History of Magnetism

Our knowledge of magnetism and magnetic phenomena is as old as science itself. According to the writings of the Greek philosopher Aristotle (384–322 B.C.), the attractive power of magnets was known by Thales of Miletus, whose life spanned the period 640?–546 B.C. It was not until the sixteenth century, however, that any significant experimental work on magnets was performed. During this century the English physician Gilbert (1544–1603) studied the properties of magnets, realized that a magnetic field existed around the earth, and even magnetized an iron sphere and showed that the magnetic field around was similar to that around the earth. Several other workers also contributed to the knowledge of magnetism during this same period.

The eighteenth century was a period of considerable growth for the theory and understanding of electrostatics. It is therefore not surprising to find that in the eighteenth century the theory of magnetism developed along lines parallel to that of electrostatics. The basic law that evolved was the inverse-square law of attraction and repulsion between unlike and like magnetic poles. Indeed, it would have been difficult for the theory to develop along any other path since batteries for producing a steady current were nonexistent. With the development of the voltaic cell by Volta (1745–1827), it was not long before the magnetic effects of currents were discovered by Oersted in 1820. This was followed by the formulation by Biot (1774–1862) and Savart (1791–1841), of the law for the magnetic field from a long straight current-carrying wire. Further studies by Ampére (1775–1836) led to the law of force between conductors carrying currents. In addition, Ampére's studies on the magnetic field from current-carrying loops led him to postulate that magnetism itself was due to circulating currents on an atomic scale. Thus the gap between the magnetic fields produced by currents and those produced by magnets was effectively closed.

Today it is expedient to base our entire theory of magnetism and static magnetic fields on the work of Biot, Savart, and Ampére. A formulation in terms of fields produced by currents or charges in motion can account for all known static magnetic effects. The magnetic effects of material bodies is accounted for by equivalent volume and surface currents. The main effort of the following sections will be devoted to the magnetic effects of currents, since this provides us with a general foundation for the understanding of all static magnetic phenomena. Ampére's law of force between two closed current-carrying conducting loops will be elevated to the position of the fundamental law or postulate from which we shall proceed.

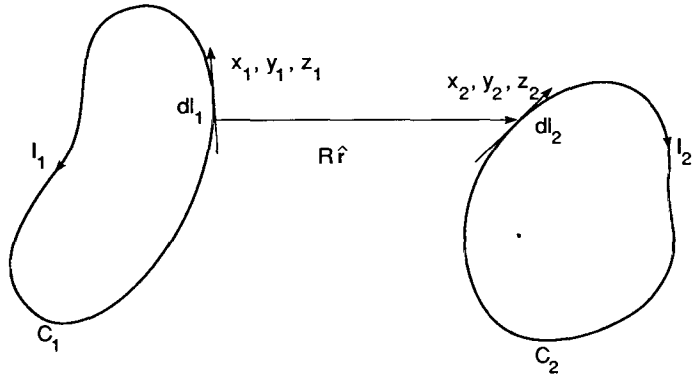

Figure 3.1. Illustration of Ampére's law of force.

3.2 The Magnetic Interaction of Steady Line Currents

The magnetic interaction of currents is best described in terms of an experimentally established interaction in vacuum that is analogous to the electrostatic Coulomb's law. The mathematical generalization of the results of Ampére's experiments, which gave the force between two current-carrying elements, as shown in Figure 3.1, is

$$\mathbf{F}_{21} = \frac{\mu_0}{4\pi} \oint_{c_1} \cdot \oint_{c_2} \cdot \frac{I_2\, d\mathbf{l}_2 \times (I_1\, d\mathbf{l}_1 \times \hat{\mathbf{r}})}{R^2} \tag{3.1}$$

The vector force F_{21} (newtons) is the force exerted on the conducting loop C_2 by C_1, as caused by the mutual interaction of the currents I_1 and I_2. The vector distance from dl_1 to dl_2 is $\mathbf{r}_2 - \mathbf{r}_1 = R\hat{\mathbf{r}}$, where $\hat{\mathbf{r}}$ is a unit vector directed from x_1, y_1, z_1 to x_2, y_2, z_2 and $R = [(x_2 - x_1) + (y_2 - y_1) + (z_2 - z_1)]^{1/2}$.

Equation (3.1) reveals the inverse-square-law relationship. The differential element of force $d\mathbf{F}_{21}$ between $I_1\, dl_1$ and $I_2\, dl_2$ may be regarded as given by the integrand in Eq.(3.1) and is

$$d\mathbf{F}_{21} = \frac{\mu_0 I_1 I_2}{4\pi R^2} d\mathbf{l}_2 \times (d\mathbf{l}_1 \times \hat{\mathbf{r}}) \tag{3.2}$$

The triple-vector product may be expanded to give

$$d\mathbf{F}_{21} = \frac{\mu_0 I_1 I_2}{4\pi R^2} [(d\mathbf{l}_2 \cdot \hat{\mathbf{r}})\, d\mathbf{l}_1 - (d\mathbf{l}_2 \cdot d\mathbf{l}_1)\, \hat{\mathbf{r}}] \tag{3.3}$$

One should note that Eqs.(3.2) or (3.3) do not correspond to a physically realizable condition since a steady-current element cannot be isolated. All steady currents must flow around continuous loops or paths since they have a zero divergence.

A further difficulty with relation (3.2) or (3.3) is that it is not symmetrical in $I_1\,dl_1$ and $I_2\,dl_2$. This superficially appears to contradict Newton's third law, which states that every action must have an equal and opposite reaction (i.e., the force exerted on $I_2\,dl_2$ by $I_1\,dl_1$ is not necessarily equal and opposite to the force exerted on $I_1\,dl_1$ by $I_2\,dl_2$). However, if the entire closed conductor, such as C_1 and C_2, is considered, no such difficulty arises and Newton's law is satisfied.

3.3 The Magnetic Induction Field

Equation (3.1) can be separated into a field force and a field,

$$\mathbf{F}_{21} = \oint_{C_2} I_2\, \mathrm{d}\mathbf{l}_2 \times \mathbf{B}_{21} \tag{3.4}$$

$$\mathbf{B}_{21} = \frac{\mu_0}{4\pi} \oint_{C_1} \frac{I_1\, \mathrm{d}\mathbf{l}_1 \times \hat{\mathbf{r}}}{R^2} \tag{3.5}$$

Equation (3.1) may be thought of as evaluating the force between current-carrying conductors through an action-at-a-distance formulation. In contrast, Eq.(3.4) evaluates the force on a current loop in terms of the interaction of this current with the magnetic field **B**, which in turn is set up by the remaining current in the system. The current-field interaction that produces $\mathbf{F}_{21}$ in Eq.(3.4) takes place over the extent of the current loop C_2, while the magnetic field $\mathbf{B}_{21}$ depends only on the current and geometry of C_1 which sets up the field.

One of the advantages of the field formulation of Eq.(3.5) is that when **B** is known, this relation permits one to evaluate the force exerted on a current-carrying conductor placed in the field **B** without consideration of the system of currents which give rise to **B**. Equation (3.5) is the law based on the experimental and theoretical work of Biot and Savart and is therefore usually called the *Biot–Savart law*. Since this law may also be extracted from Ampére's law of force, it is sometimes referred to as *Ampére's law* as well.

A charge q moving with a velocity v is equivalent to an element of current $I\,dl = q\mathbf{v}$ and hence in the presence of a magnetic field experiences a force **F** given by

$$\mathbf{F} = q\mathbf{v} \times \mathbf{B} \tag{3.6}$$

This force is called the *Lorentz force*, and Eq.(3.6) is often taken as the defining equation for **B**.

In practice, one does not always deal with currents flowing in thin conductors, and hence it is necessary to generalize the defining Eq.(3.5) for **B** so that it will apply for any arbitrary volume distribution of current. The steady-current flow field does not diverge, and all flow lines form

closed loops. If the direction is associated with a current density **j**, rather than a short length $d\mathbf{l}$, then the total current is $\mathbf{j}\,dS$, where dS is the differential cross-sectional area through which the current flows. The total current contained in a volume V will therefore produce a field **B** given by

$$\mathbf{B} = \frac{\mu_0}{4\pi} \int_v \frac{\mathbf{j} \times \hat{\mathbf{r}}}{R^2}\, dV \tag{3.7}$$

where the integration is over all source coordinates x, y, and z and dV is an element of volume $dS\,dl$. For a surface current $\mathbf{j}_s$ amperes per meter flowing on a surface S, a similar derivation shows that the field produced is given by

$$\mathbf{B} = \frac{\mu_0}{4\pi} \int_s \frac{\mathbf{j}_S \times \hat{\mathbf{r}}}{R^2}\, dS \tag{3.8}$$

The use of Eqs.(3.4), (3.5), (3.7), or (3.8) is mathematically cumbersome for all but the simplest geometries. For this reason, three-dimensional computer codes utilizing Eqs.(3.4) and (3.5) are generally called upon to determine the forces and magnetic fields associated with complex conductor geometries.

A particularly useful technique for solving magnetostatic problems having cylindrical geometry makes use of Ampére's circuital law,

$$\int_s \nabla \times \mathbf{B} \cdot d\mathbf{S} = \int_s \mu_0\, \mathbf{j} \cdot d\mathbf{S} = \oint_c \mathbf{B} \cdot d\mathbf{l} \tag{3.9}$$

This equation states that the line integral of $\mathbf{B} \cdot d\mathbf{l}$ around any closed contour C is equal to μ_0 times the total net current passing through the contour C.

3.3.1 Field from an Infinite Conductor of Finite Radius

Consider an infinite conductor of radius a with total current I (Figure 3.2). The current density j is equal to $I/\pi a^2$ and is uniform over the cross section of the conductor. From symmetry considerations the field **B** only has a component B_ϕ, which is a function of r only. Using Ampére's circuital law Eq.(3.9) and integrating around a circular contour of radius r gives

$$\oint B_\phi\, dl = \int_0^{2\pi} B_\phi\, r\, d\phi = \mu_0 \int_0^r \cdot \int_0^{2\pi} j\, r\, d\phi\, dr = \frac{\mu_0 I}{\pi a^2} \int_0^r \cdot \int_0^{2\pi} r\, d\phi\, dr \qquad r \le a$$

or

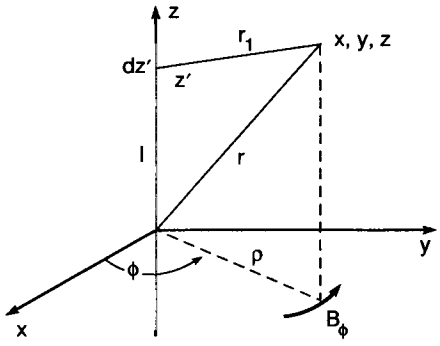

Figure 3.2. An infinitely long wire with a current I and self-consistent field B_ϕ.

$$B_\phi = \frac{\mu_0 I r}{2\pi a^2} \quad r \leq a \tag{3.10}$$

For $r \leq a$, the total current enclosed is I, so

$$\int_0^{2\pi} B_\phi r \, d\phi = \mu_0 I$$

or

$$B_\phi = \frac{\mu_0 I}{2\pi r} \quad r \geq a \tag{3.11}$$

A plot of the intensity of B_ϕ as a function of r is given in Figure 3.3.

3.3.2 Force Between Two Infinite Conductors

Consider two thin infinite conductors which are parallel and spaced at a distance d. The currents flowing in the conductors are I_1 and I_2 as in Figure 3.4. From Eq.(3.11) the magnetic field at C_2 due to C_1 has a ϕ component only and is given by

$$B_\phi = \frac{\mu_0 I_1}{2\pi d} \tag{3.12}$$

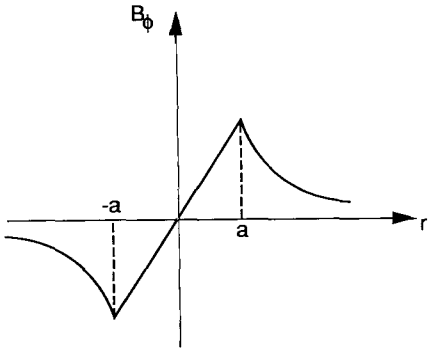

Figure 3.3. Magnetic field variation across a plasma filament of radius $2a$.

The force exerted on C_2 per unit length is given by Eq.(3.4) and is

$$\mathbf{F}_{21} = I_2 \hat{\mathbf{z}} \times B_\phi \hat{\boldsymbol{\phi}} = \frac{-\mu_0 I_1 I_2}{2\pi d} \hat{\mathbf{r}} \tag{3.13}$$

When I_1 and I_2 are in the same direction, the two conductors experience an attractive force. When I_1 and I_2 are oppositely directed, the conductors repel each other.

The fact that two straight parallel conductors exert forces of attraction or repulsion on one another is made the basis of the definition of the ampere in the mks system. The ampere is defined as follows:

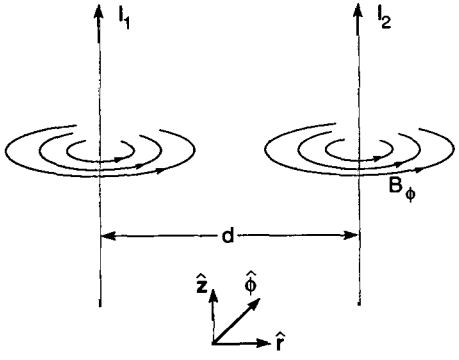

Figure 3.4. Two parallel current-carrying filaments.

One ampere is that unvarying current which, if present in each of two parallel conductors of infinite length and one meter apart in empty space, causes each conductor to experience a force of exactly 2×10^{-7} newtons per meter of length.

It follows from this definition that the numerical value of μ_0 in the rationalized mks system, is exactly $4\pi \times 10^{-7}$ or, to four significant figures, $\mu_0 = 12.57 \times 10^{-7}$ webers/amp-m.

3.4 The Vector Potential

If, in Eq.(3.7), we replace $\hat{\mathbf{r}}/R^2$ by $-\nabla(1/R)$, the integrand becomes $-\mathbf{j} \times \nabla(1/R)$. The vector differential operator ∇ affects only the variables x, y, and z, and since $\mathbf{j}$ is a function of the source coordinate x', y', z' only, this latter relation may also be written as follows: $-\mathbf{j} \times \nabla(1/R) = \nabla \times (\mathbf{j}/R)$ [and $\nabla \times (\mathbf{j}/R) = (1/R)\nabla \times \mathbf{j} - \mathbf{j} \times \nabla(1/R) = -\mathbf{j} \times \nabla(1/R)$] since $\nabla \times \mathbf{j} = 0$. Thus, in place of Eq.(3.7) we may write

$$\mathbf{B}(x,y,z) = \nabla \times \frac{\mu_0}{4\pi} \int_v \frac{\mathbf{j}(x',y',z')}{R} dV \tag{3.14}$$

Equation (3.14) expresses the field $\mathbf{B}$ at the point (x,y,z) as the curl of a vector potential function given by the integral. From Eq.(3.14), the definition of the vector potential function, denoted by $\mathbf{A}$, is

$$\mathbf{A}(x,y,z) = \frac{\mu_0}{4\pi} \int_v \frac{\mathbf{j}(x',y',z')}{R} dV \tag{3.15}$$

The integral for $\mathbf{A}$ is a vector integral and must be evaluated by decomposing the integrand into components along the coordinate axis. Having computed $\mathbf{A}$, the field $\mathbf{B}$ is obtained by taking the curl of $\mathbf{A}$:

$$\mathbf{B} = \nabla \times \mathbf{A} \tag{3.16}$$

The integral for $\mathbf{A}$ is easier to evaluate than the original expression Eq.(3.7) for $\mathbf{B}$, and since the curl operation is readily performed, the use of Eq.(3.15) as an intermediate step provides us with a simpler procedure for finding $\mathbf{B}$.

3.4.1 Field from a Circular Loop and Force Between Two Circular Loops

Consider a circular conducting loop carrying a current I. The radius of the loop is a and it is located in the xy plane at the origin, as in Figure 3.5. Of course a seat of electromotive force (emf) is necessary to maintain the current, and one may either imagine the turn cut and a small seat of emf

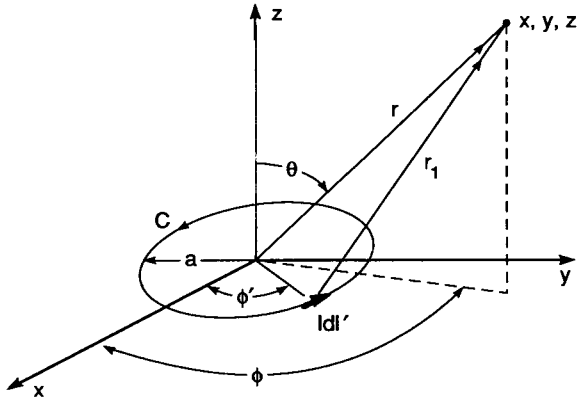

Figure 3.5. A circular current loop.

inserted, or consider that current is led into and out of the turn through two wires side by side. Using Eq.(3.15), we must evaluate the following integral:

$$\mathbf{A} = \frac{\mu_0 I}{4\pi} \oint_C \frac{d\mathbf{l}'}{r_1} \tag{3.17}$$

where in this case

$$d\mathbf{l}' = \hat{\phi}\, a\, d\phi' = \left(-\hat{\mathbf{x}} \sin\phi' + \hat{\mathbf{y}} \cos\phi'\right) a\, d\phi' \tag{3.18}$$

$$\mathbf{r}_1 = \hat{\mathbf{x}}\left(x - a\cos\phi'\right) + \hat{\mathbf{y}}\left(y - a\sin\phi'\right) + \hat{\mathbf{z}}\, z \tag{3.19}$$

The expression for r_1 is

$$r_1 = \left[\left(x - a\cos\phi'\right)^2 + \left(y - a\sin\phi'\right)^2 + z^2\right]^{1/2}$$

$$= \left(x^2 + y^2 + z^2 + a^2 - 2ax\cos\phi' - 2ay\sin\phi'\right)^{1/2}$$

$$\approx r\left(1 - \frac{2ax}{r^2}\cos\phi' - \frac{2ay}{r^2}\sin\phi'\right)^{1/2} \tag{3.20}$$

since $r^2 >> a^2$. For r_1^{-1} we have approximately

$$r_1^{-1} \approx r^{-1}\left(1 + \frac{ax}{r^2}\cos\phi' + \frac{ay}{r^2}\sin\phi'\right) \tag{3.21}$$

by using the binomial expansion and retaining only the leading terms. The integral for **A** becomes

$$\mathbf{A} = \frac{\mu_0 I\,\pi\,a}{4\pi\,r}\int_0^{2\pi}\left(-\hat{\mathbf{x}}\sin\phi' + \hat{\mathbf{y}}\cos\phi'\right)\left(1 + \frac{a\,x}{r^2}\cos\phi' + \frac{a\,y}{r^2}\sin\phi'\right)d\phi' \tag{3.22}$$

and integrates to give

$$\mathbf{A} = \frac{\mu_0\, I\,\pi\,a^2}{4\pi\,r^3}(-\hat{\mathbf{x}}y + \hat{\mathbf{y}}x) \tag{3.23}$$

Referred to a spherical coordinate system, **A** is given by

$$\mathbf{A} = \left(\mathbf{A}\cdot\hat{\mathbf{r}}\right)\hat{\mathbf{r}} + \left(\mathbf{A}\cdot\hat{\boldsymbol{\phi}}\right)\hat{\boldsymbol{\phi}} + \left(\mathbf{A}\cdot\hat{\boldsymbol{\theta}}\right)\hat{\boldsymbol{\theta}} = \frac{\mu_0\, I\,\pi\,a^2}{4\pi\,r^2}\sin\theta\,\hat{\boldsymbol{\phi}} = A_\phi\hat{\boldsymbol{\phi}} \tag{3.24}$$

so that, from Eq.(3.16)

$$\mathbf{B} = \frac{\mu_0\, I\,\pi\,a^2}{4\pi\,r^3}\left(\hat{\mathbf{r}}\,2\cos\theta + \hat{\boldsymbol{\theta}}\sin\theta\right) \tag{3.25}$$

3.4.2 Force Between Two Circular Loops Lying in a Plane

In the plane of the loops, $\theta = \pi/2$, so that $\mathbf{B}_{21} = \hat{\boldsymbol{\theta}}\,\mu_0\, I\, a^2 / 4\, r^3$, and Ampére's law of force gives

$$\mathbf{F}_{21} = \mathbf{I}_2 \times \mathbf{B}_{21} = \hat{\boldsymbol{\phi}}\, I_2 \times \left(-\hat{\boldsymbol{\theta}}\,\frac{\mu_0\, I_1\, a^2}{4r^3}\right) = \hat{\mathbf{r}}\left(\frac{\mu_0 I_1 I_2 a^2}{4r^3}\right) \tag{3.26}$$

3.5 Quasi–Stationary Magnetic Fields

To complete a discussion of magnetostatics, it is necessary to derive an expression for the stored magnetic energy in a cosmic network. This will then make a full discussion of inductance and also a more powerful technique for determining forces between current-carrying circuits, possible. In order to determine an expression for stored magnetic energy due to time-stationary currents, it is necessary to know something about time-varying currents and time-varying magnetic fields. Consequently, this section starts with a statement about Faraday's law of induction.

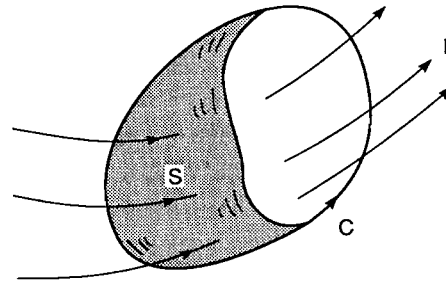

Figure 3.6. Illustration of Faraday's law.

3.5.1 Faraday's Law

If we consider any closed stationary path in space which is linked by a changing magnetic field, it is found that the induced voltage around this path s is equal to the negative time rate of change of the total magnetic flux through the closed path. Let C denote a closed path as in Figure 3.6. The induced voltage around this path is given by the line integral of the induced electric field around C and is

$$\phi = \oint_C \mathbf{E} \cdot \mathbf{dl} \tag{3.27}$$

The magnetic flux through C is given by

$$\psi = \int_s \mathbf{B} \cdot \mathbf{dS} \tag{3.28}$$

where S is any surface with C as its boundary. Thus the mathematical statement of Faraday's law is

$$\oint_C \mathbf{E} \cdot \mathbf{dl} = -\frac{\partial}{\partial t} \int_S \mathbf{B} \cdot \mathbf{dS} \tag{3.29}$$

Basically, the law states that a changing magnetic field will induce an electric field. The induced electric field exists in space regardless of whether a conductor exists or not. When a conducting path is present, a current will flow, and we refer to this current as an induced current. Faraday's law is the principle on which most electric generators operate. Note that the electric field set up by a changing magnetic field is nonconservative, as Eq.(3.29) clearly indicates. The changing magnetic field becomes a source for an electric field.

3.5.2 Motion Induced Electric Fields

Whenever a conductor moves through a static magnetic field, a voltage is induced across the conductor. This voltage is in addition to that calculated by Eq.(3.29). The magnitude of this voltage may be found from the Lorentz force Eq.(3.6). The force is seen to act in a direction perpendicular to both v and **B**. The interpretation of the Lorentz force gives rise to the concept that an observer moving through a static magnetic field also sees, in addition to the magnetic field, an electric field. A unit of charge moving with the observer appears to be stationary, and any force experienced by that charge is ascribed to the existence of an electrostatic field. But a force is experienced and is given by Eq.(3.6). Consequently, in the moving reference frame, this fact is interpreted as revealing the existence of an electric field **E** given by

$$\mathbf{E} = \frac{\mathbf{F}}{q} = \mathbf{v} \times \mathbf{B} \tag{3.30}$$

Equation (3.30) gives an alternative and more general method of evaluating the induced voltage in a moving conductor.

As an example consider a a cylindrical conductor moving with a velocity v through a uniform field **B**, as in Figure 3.7, where **B** is orthogonal to v. Each electron in the conducting medium experience a force $F = -evB$ which tends to displace the electrons along the conductor in the direction shown. When an equilibrium state is reached, the process stops, and the conductor is left polarized as shown with an electrostatic force equal and opposite to the Lorentz force. In this case, $E = -vB$. The induced voltage between the ends of the conductor is defined by

$$\phi = \int_{P_1}^{P_2} \mathbf{E} \cdot \mathbf{dl} \tag{3.31}$$

The induced voltage caused by motion of a conductor through a magnetic field is called motional emf .

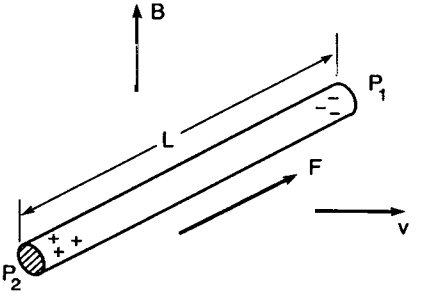

Figure 3.7. Induced voltage (potential drop between P_2 and P_1) in a conductor moving across a magnetic field.

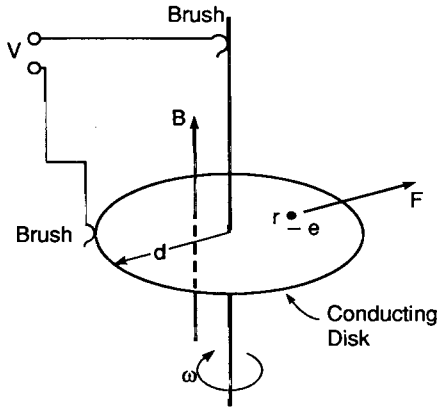

Figure 3.8. The Faraday disk dynamo. A potential ϕ = V is produced at the terminals.

3.5.3. Faraday Disk Dynamo

The Faraday disk dynamo is illustrated in Figure 3.8. It consists of a circular conducting disk rotating in a uniform magnetic field **B**. Brushes make contact with the disk at the center and along the periphery. The magnitude of the induced voltage is found from the Lorentz force, Eqs.(3.30) and (3.31). An electron at a radial distance r from the center has a velocity ωr and hence experiences a force $e\omega rB$ directed radially outward. The electric field acting on the electron at equilibrium is also ωrB but is directed radially inward. The potential from the center to the outer rim of the disk is thus

$$\phi = \int_0^d E(r)\, dr = -\omega B \int_0^d r\, dr = -\frac{\omega B d^2}{2} \tag{3.32}$$

The value computed from Eq.(3.32) is the open-circuit voltage of the Faraday disk dynamo and therefore also represents the emf of the generator.

3.6 Inductance

Consider a single current-carrying loop in which a constant current has been established. This current produces a magnetic field. If the current is caused to change, so will the magnetic field. But this means that the total flux linking the loop also changes and, by Faraday's law, a voltage is induced in the loop. The self-induced voltage always has a polarity that tends to oppose the original change in current. For example, if the current begins to decrease, the induced voltage acts in a direction to offset this decrease. This property of a single circuit is known as self-inductance.

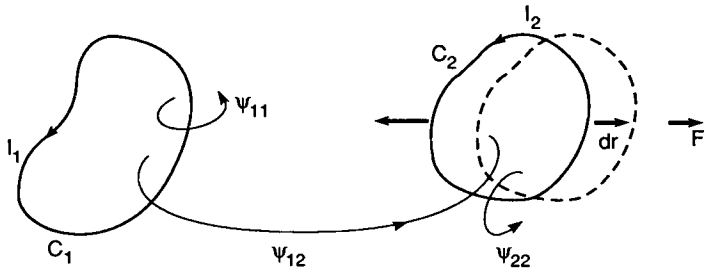

Figure 3.9. Illustration of two circuits and their relative displacement (L_{12} negative).

The similar effect of a changing current in one circuit producing an induced voltage in another circuit is known as mutual inductance.

Mathematically, inductance may be defined in terms of flux linkages. If ψ_{12} is the magnetic flux linking circuit C_2 due to a current I_1 flowing in circuit C_1 (Figure 3.9), the mutual inductance L_{12} between circuit C_1 and C_2 is defined by

$$L_{12} = \frac{\text{flux linking } C_2 \text{ due to current in } C_1}{\text{current in } C_1} = \frac{\psi_{12}}{I_1} \tag{3.33}$$

The self inductance L_{11} of circuit C_1 is defined in a similar way; that is,

$$L_{11} = \frac{\text{flux linking } C_1 \text{ due to current in } C_1}{\text{current in } C_1} = \frac{\psi_{11}}{I_1} \tag{3.34}$$

The mutual inductance between C_1 and C_2 may be defined by

$$L_{21} = \frac{\psi_{21}}{I_2} \tag{3.35}$$

It can be shown that $L_{12} = L_{21}$ so that Eqs.(3.33) and (3.35) are equivalent. This is a statement of the *reciprocity theorem.*

The above definition of inductance is satisfactory only for quasi-stationary magnetic fields where the current and the magnetic field have the same phase angle over the whole region of the circuit. At high frequencies the magnetic field does not have the same phase angle over the whole region of the circuit because of the finite time required to propagate the effects of a changing current and field through space. A more general definition in terms of the magnetic energy associated with a circuit will be given in the following section.

3.7 Storage of Magnetic Energy

3.7.1 Energy in a System of Current Loops

The energy W_B stored in the magnetic field of N current filaments is given by

$$W_B = \frac{1}{2} \sum_{i=1}^{N} \sum_{j=1}^{N} L_{ij} I_i I_j \tag{3.36}$$

or, in terms of the magnetic flux, by

$$W_B = \frac{1}{2} \sum_{i=1}^{N} \psi_i I_i \tag{3.37}$$

where I_i is the current flowing in the ith filament and ψ_i is the flux linking the ith filament due to all the other current filaments in the current loop. This in turn is given by

$$\psi = \sum_{\substack{j=1 \\ j \neq i}}^{N} L_{ij} I_j \tag{3.38}$$

In terms of field energy, the inductance may be defined by the equation

$$W_B = \frac{1}{2} L I^2 \tag{3.39}$$

so that

$$L = \frac{2 W_B}{I^2} \tag{3.40}$$

This definition is often easier to apply in practice in order to evaluate L than the original definition in terms of flux linkages. The quality of a circuit that allows the storage of magnetic energy is called inductance. In terms of the field integral the magnetic energy Eq.(3.39) is

$$W_B = \frac{1}{2} \int_V \mathbf{B} \cdot \mathbf{H} \, dV = \frac{1}{2\mu} \int_V \mathbf{H} \cdot \mathbf{H} \, dV \tag{3.41}$$

3.7.2 *In Situ* Storage in Force Free Magnetic Field Configurations

The storage of energy in the force-free magnetic field (Section 1.7.2) can be thought of as a slow process where the field evolves through a sequence of force-free configurations, each time ending up in a higher energy state [Tandberg-Hansson and Emslie 1988]. An example of this slow process is in the photosphere and lower chromosphere of the Sun, where the energy of the plasma motion dominates the magnetic energy and, therefore, the field is swept passively along with the plasma. This situation is characterized as a high-β plasma; i.e., the parameter

$$\beta = \frac{\text{gas pressure}}{\text{magnetic pressure}} = \frac{2\mu_0 nkT}{B^2} \tag{3.42}$$

is large ($\beta >> 1$). Higher up in the corona where the density is so small that the magnetic pressure dominates, we have a low-β plasma, and the magnetic field must take on a force-free character [Gold 1964] as it slowly evolves. This magnetohydrodynamic (MHD) process is possible since the timescale for the "wind-up" is days or weeks, while the field adjustment at any stage takes place with the Alfvén speed Eq.(2.19), leading to timescales of the order of seconds.

If α is constant in time and space, we can take the curl of Eq.(1.12) and find

$$\nabla^2 \mathbf{B} + \alpha^2 \mathbf{B} = 0 \tag{3.43}$$

which is the vector Helmholtz equation. This linear problem then is completely solvable [Chandrasekhar and Kendall 1957, Ferraro and Plumpton 1966, Nakagawa and Raadu 1972].

Using Eq.(3.43) and the observed boundary conditions in the form of the value of the longitudinal magnetic field (from magnetograph observations), we can compute the structure of the force-free field and the resulting stored magnetic energy. In these cases, α is adjusted until reasonable agreement is obtained with observations. With the availability of complete vector magnetic field observations, the field calculations have improved since α can be determined with higher precision from Eq.(1.12) with the expression

$$\alpha = \frac{(\nabla \times \mathbf{B}) \cdot \mathbf{B}}{B^2} \tag{3.44}$$

In general, the parameter α is not constant in space and time, that is

$$\alpha = \alpha(\mathbf{r}, t) \tag{3.45}$$

so that Eq.(3.43) is nonlinear, and the problem must be solved by computer simulation.

3.8 Forces as Derivatives of Coefficients of Inductance

The force between separate current-carrying loops or circuits may be evaluated by Ampére's law of force. However, an alternative method that is much easier to apply in many cases may also be used. This alternative method essentially consists of evaluating the derivatives of mutual-inductance coefficients with respect to arbitrary virtual displacements of the circuits with respect to each other (see, e.g., Figure 3.9). When circuits are displaced relative to each other, the mutual inductance, and hence the energy stored in the magnetic field, changes. The change in the magnetic energy is in turn related to the work done against the forces of the field in displacing the circuits.

If we have N circuits and displace the jth circuit by an amount dr_j, the force F_j exerted on C_j by all the other circuits is given by

$$F_j = \sum_{\substack{n=1 \\ n \neq j}}^{N} I_j I_n \frac{dL_{jn}}{dr_j} \tag{3.46}$$

where F_j is the component of force along dr_j acting on the jth circuit.

Example 3.1 Force on two parallel filaments. Consider two thin infinitely long conducting filaments as in Figure 3.4. The filaments are separated by a distance D. The currents in the two filaments are I_1 and I_2. The flux linking C_2 due to the current I_1 in C_1 is

$$\psi_{12} = \frac{\mu_0 I_1}{2\pi} \int_D^\infty \frac{dx}{x} \qquad \text{per unit length}$$

From Eq.(3.46) the force per unit length exerted on C_2 by C_1 is

$$F = I_1 I_2 \frac{dL_{12}}{dD}\bigg|_{I=\text{constant}} = I_2 \frac{d\psi_{12}}{dD} = -\frac{\mu_0 I_1 I_2}{2\pi D}$$

in accord with Eq.(3.13) obtained using Ampére's law.

3.9 Measurement of Magnetic Fields in Laboratory Plasmas

B-Dot Probes. The simplest way to measure the magnetic field in the vicinity of a point in space is to use a small coil of wire (Figure 3.10). In a uniform, time-varying magnetic field, the voltage induced in the coil is

$$\Phi = NA\dot{B}$$

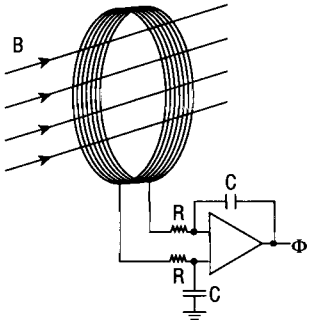

Figure 3.10. B–Dot probe and integrating circuit.

where N is the number of turns in the coil of area A and the dot denotes the time derivative of B. If B, rather than $\dot{B}$, is the desired quantity, an integrating circuit may be used to obtain a voltage proportional to the field

$$\Phi = \frac{NAB}{RC}$$

where RC is the time constant of the integrator.

Rogowski Coil. Many different variations of the B-dot probe are available. One of the most widespread is the Rogowski coil. This is a solenoidal coil whose ends are brought around together to form a torus as shown in Figure 3.11a. Consider a coil of uniform cross sectional area A with a constant number of turns per unit length n. If the magnetic field varies little over a one-turn spacing, i.e., $|\nabla B|/B << n$, the total flux linkage by the coil Eq.(3.28) can be written as an integral over the individual turns:

$$\psi = n \oint_l \cdot \int_A \mathbf{B} \cdot d\mathbf{l}\, dA$$

where $d\mathbf{l}$ is the line element along the solenoidal axis as depicted in Figure 3.11b. The purpose of the return wire threading the loops is to exclude the contribution of flux passing through the torus center. Changing the order of integration and using Eq.(3.9) gives

$$\psi = nA\mu_0 I$$

The signal voltage from the Rogowski coil is then

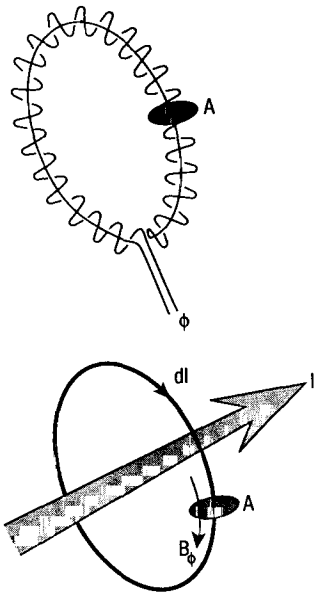

Figure 3.11. (top) Rogowski coil. **(bottom)** Equivalent geometry for the integral form of flux through a Rogowski coil.

$$\phi = d\psi/dt = nA\mu_0 \dot{I}$$

The Rogowski coil provides a direct measurement of the total current, particle and displacement, flowing through its center. Its signal is independent of the distribution of the current within the loop. The merit of the Rogowski coil is that it need not come into contact with the current whose field it measures. This is an important consideration for intense relativistic electron beams.

Internal Magnetic Field Probes. It is often possible to use internal sensing coils in tenuous nonenergetic plasmas. Stenzel and Gekelman (1981) have used such probes with great success to measure the time evolution of magnetic fields in all three dimensions in plasmas contained in large vacuum chambers.

3.10 Particle-in-Cell Simulation of Interacting Currents

The basic geometry under study is shown in Figure 3.12. This figure depicts two current-conducting plasma filaments aligned along a magnetic field $\mathbf{B}_0$ and separated by a distance comparable to the diameters of the filament. The plasma is charge neutral $n_e = n_i$ and initially thermalized at a temperature $v_{th\,x} = v_{th\,y} = v_{th\,z}$ for both ions and electrons. The density distribution across a column may either be a flat profile, a Bennett profile, a Gaussian profile, or any arbitrary profile

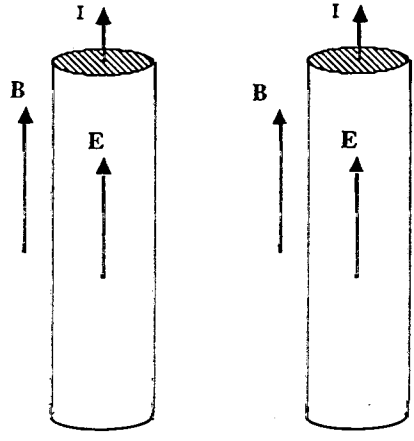

Figure 3.12. Basic geometry under analysis: two parallel Birkeland currents formed by the tendency of charged particles to follow magnetic lines of force **B** and to pinch due to their own induced magnetic field.

$n_{e,i}(r)$. The conduction of current is initiated by placing an electric field $\mathbf{E} = \mathbf{E}_0$ along each column. This then produces a current which increases with time. Whether or not a filament pinches, or is simply confined by the self-consistent azimuthal magnetic field B_ϕ, depends on the strength of $\mathbf{E}_0$.

Solution of the relative motion of the two filaments and their reconfiguration by the Biot–Savart forces requires a 3D particle-in-cell treatment. The codes SPLASH and TRISTAN have been applied to this geometry (Chapter 8).

3.10.1 Simulation Setup

We choose a temperature typical of cosmic Birkeland filaments, a few kiloelectronvolts, by setting the initial dimensionless simulation parameters (Section 8.8) to $\omega_p\, dt = 0.25$, $\lambda_D / \Delta = 0.25$, and $c\, dt / \Delta = 1.0$. A field-aligned Birkeland filament is established by means of the parameter $\omega_{c\,0} / \omega_p = 1.5$. For this choice of parameters, $\beta_{th} = 0.0625$ [Eq.(8.19)] and, for $T_e = T_i$, $\beta_p = 0.0069$ [Eq.(8.20)]. Current flow within the filaments is initiated by setting $E_z / B_z = 0.01$ c, so that $0 \le \beta_z \le 1$ [Eq.(8.18)].

For SPLASH, the radius of each filament is 3Δ and the center-to-center separation is 11Δ, while for TRISTAN the radius and separation are 12Δ and 44Δ, respectively. (Because of the spline interpolation technique, the particle space-time resolution is approximately eight times better than the cell width Δ.)

3.10.2 Initial Motion of Current Filaments

Initially, the Biot–Savart force between filaments conducting I_z currents can be approximated by Eq.(3.13). However, because of the axial magnetic field $\mathbf{B}_0$, the particles spiral as they drift or accelerate in the z–direction, thereby producing a generalized current $\mathbf{I} = \hat{z}\, I_z + \hat{\phi}\, I_\phi$. The force between the I_ϕ currents can be approximated by Eq.(3.26). Figure 3.13 illustrates the total Biot–

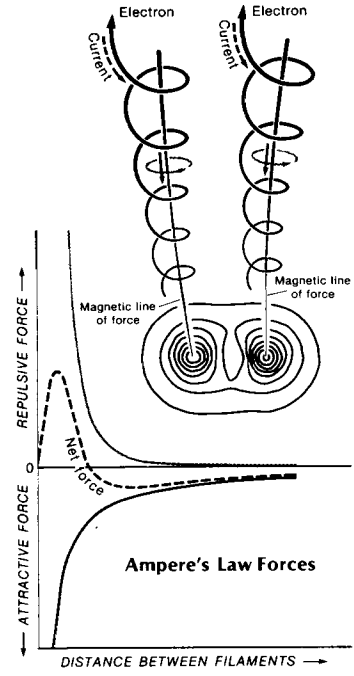

Figure 3.13. The forces between two adjacent Birkeland currents. The parallel components of current (dark gray lines) are long-range attractive, while the counter-parallel azimuthal currents (light gray rings) are short-range repulsive. A third force, long range electrostatic repulsion, is found if the electrons and ions are not present in equal numbers. These forces cause the currents to form sheets, filaments, or "magnetic ropes" and they can be found far from the source region. A projection of the current-induced magnetic fields is shown above the graph.

Savart force as a function of the spacing between helical current filaments. As shown, the electromagnetic forces between filaments are ordered as $-R_{12}^{-1}$ (long-range attractive) and R_{12}^{-3} (short range repulsive).

During long-range attraction, the motion of either filament may be approximately described by the equation

$$M\frac{d^2r}{dt^2}=\frac{\mu_0 I_z^2 L}{4\pi(a-r)} \tag{3.47}$$

whose velocity solution is

$$v = \frac{dr}{dt} = I_z \left(\frac{\mu_0 L}{2\pi M}\right)^{1/2} \left[\ln\left(\frac{a}{a-r}\right)\right]^{1/2} \tag{3.48}$$

where L is the length of the filament region involved in Biot–Savart attraction, M is the total mass, $2a$ is the distance of separation between filaments. If the filaments are sufficiently separated so that the logarithmic correction is of order unity, Eq.(3.48) is approximately given by

$$v = I_z \left(\frac{\mu_0 L}{2\pi M}\right)^{1/2} \quad \left\{ v = I_z \left(\frac{2L}{c^2 M}\right)^{1/2} = \frac{B_\phi d}{2}\sqrt{\frac{2L}{M}} \right\}_{cgs} \tag{3.49}$$

In dimensionless gaussian simulation units, Eq.(3.49) is

$$\mathbf{v} = \frac{\mathbb{B}_\phi \mathbf{d}}{2}\sqrt{\frac{2\mathbb{L}}{\mathbb{M}}} \tag{3.50}$$

where $\mathbb{M} = N_c \left(n_e/\Delta^3\right)(m_i/m_e + 1)\pi \mathbf{r}_c^2 \mathbb{L}$ and N_c are the total simulation mass and number of interacting simulation filaments, respectively. The parameter $\mathbf{d} = d/\Delta$ is the distance between filaments and $\mathbf{r_c} = r_c/\Delta$ is the radius of a filament, both given in cell widths.

3.10.3 Polarization Forces

In the presence of an axial field $\mathbf{B}_0$, the electrons gyrate in a counter clockwise direction while the ions gyrate in a clockwise direction. The relationship between the ion and electron gyroradii is $r_{Li} = (m_i / m_e)\, r_{Le} >> r_{Le}$. In addition to the gyration, the charged particles experience a polarizing force caused by the net motion of the plasma filaments across the guide field $\mathbf{B}_0$. The net motion derives from Eq.(3.49) which causes a $\mathbf{v}\times\mathbf{B}$ force, primarily in the $\pm y$–directions in adjacent filaments as shown in Figure 3.14a. As a result, the electrons in columns 2 and 1 are accelerated in the $\pm y$–directions, respectively. This leaves a net excess of the heavier ions in the original filament positions, and thereby produces, via Eq.(1.3), an electric field which opposes a further diffusion of electrons. The electrons can separate from the ions about a Debye length $\lambda_D = \sqrt{\varepsilon_0 kT / n_e e^2}$ before they are restrained by the ions. The ions then follow the electrons in a process known as ambipolar diffusion [Rose and Clark 1961]. It is evident that the dimensions of the plasma be much larger than the Debye length for ambipolar diffusion to take place. Figure 3.14b depicts the displacement of the currents in the filaments (because of excess of axial current-conducting electrons at the $\pm y$ surfaces) caused by the inward motion of the filaments across $\mathbf{B}_0$. The net result of the juxtapositioned currents I_z is a clockwise torque on the plasma filaments (Figure 3.14c).

3.10.4 Magnetic Energy Distribution and Magnetic Isobars

The two parallel axial currents produce the magnetic energy isobars [through Eq.(1.2)] shown in the time sequence of Figure 3.15. At $T=9$, the contours of B^2 are very nearly symmetric about each filament. Since the currents increase with time (because of the constant field E_z), the B^2 isobars move out from each filament until a linear superposition of isobars produce a magnetic minimum

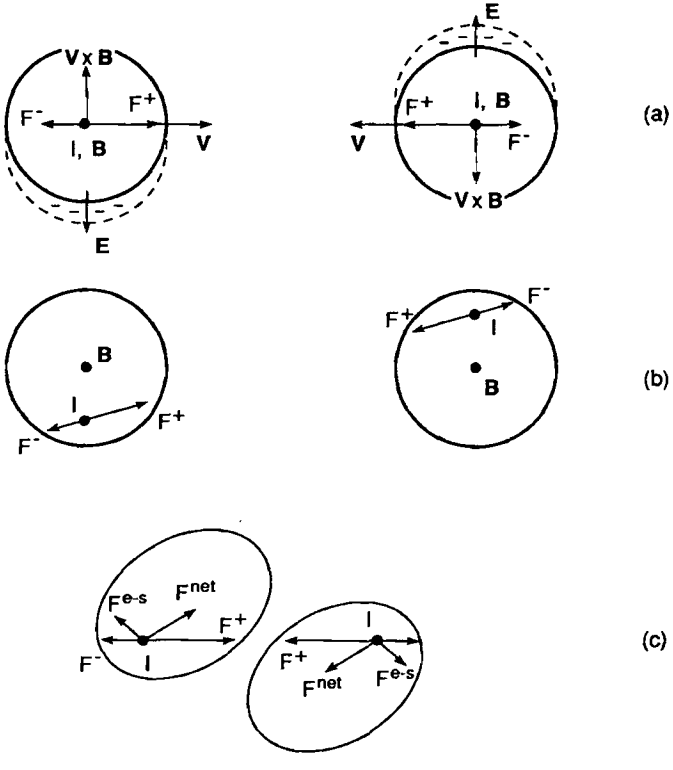

Figure 3.14. Net motion between adjacent Birkeland currents. **(a)** Polarization fields **E** due to $\mathbf{v} \times \mathbf{B}$ forces. **(b)** Net forces at early time **(c)** Net forces during filament distortion.

("sump") or core between the two filaments (Figures 3.15 and 3.16). The core has the shape of an ellipse. The effect of the net inward motion is already seen at timestep 16 with the juxtapositioning of the B^2 isobaric peaks associated with the axial currents.

In addition to the magnetic peaks and core, two narrow magnetic channels form on either side of the core (Figure 3.17). At T=255, the field strength squared in the vicinity of the core is $\mathbb{B}^2 = 0.33$. The field induced pressure is

$$p_B = (2\mu_0)^{-1} \mathbb{B}^2 \tag{3.51}$$

At time T=255, a channel exists only on the right-hand-side of Figure 3.17 with length 9 Δ' and width 0.5 Δ' to 2.0 Δ' (The channel alternates from right to left with the passage of time [Peratt 1986]. The velocity of the isobars toward the core is, approximately, 0.032 cells per timestep, or

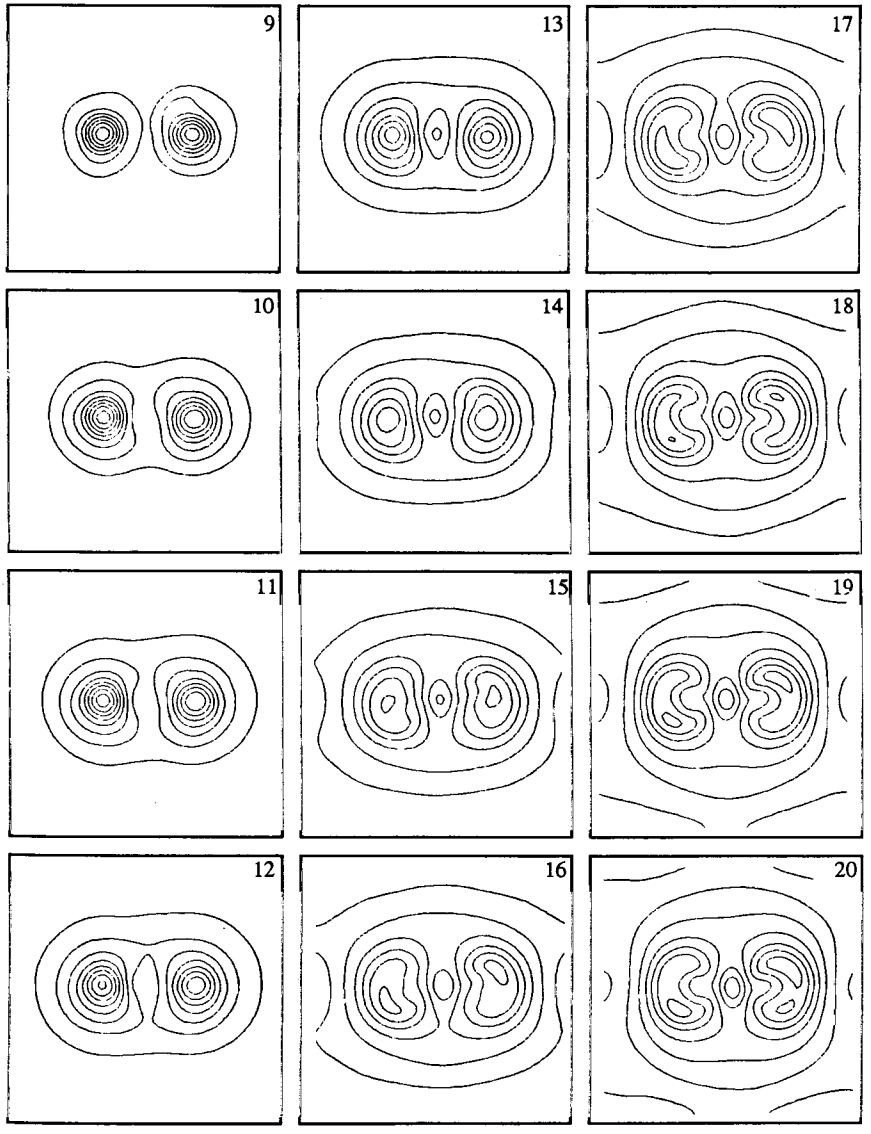

Figure 3.15. Contours of magnetic energy B^2 about two adjacent filaments at the simulation cross-section. $T = 9$–20 in 1 ΔT steps. The contours at the locations of the two filaments correspond to energy maxima while the central ellipse is an energy minimum. "Hot spots" in azimuthal field energy feeding synchrotron radiation are beginning to become noticeable in later time frames.

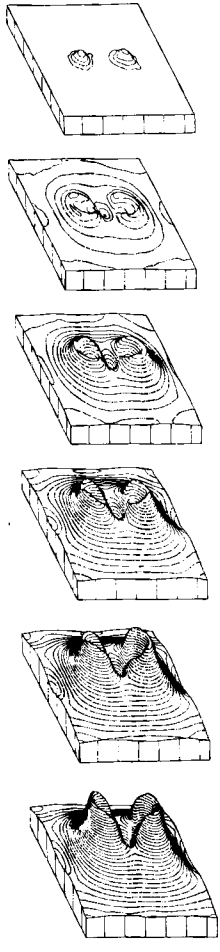

Figure 3.16. Isometric view of magnetic energy contours of Figure 3.15. Time increases from top to bottom.

$$v_{comp} = 0.032\ \Delta' / dt' \tag{3.52}$$

Because of the inward traveling isobars, plasma external to the two conducting currents is swept into both the channel and the core. Part of this external plasma derives from unpinched plasma which conducts the current before the Bennett relation Eq.(1.9) is established.

The phenomena described in the simulation is observed in the laboratory. Figure 3.18 shows laser Schlieren photographs taken at two different times of two interacting Z pinches. The Z pinches were created by stringing two 2 cm long wires between an anode and cathode of a pulsed power generator (Figure 2.9), which then exploded into plasma pinches with the conduction of

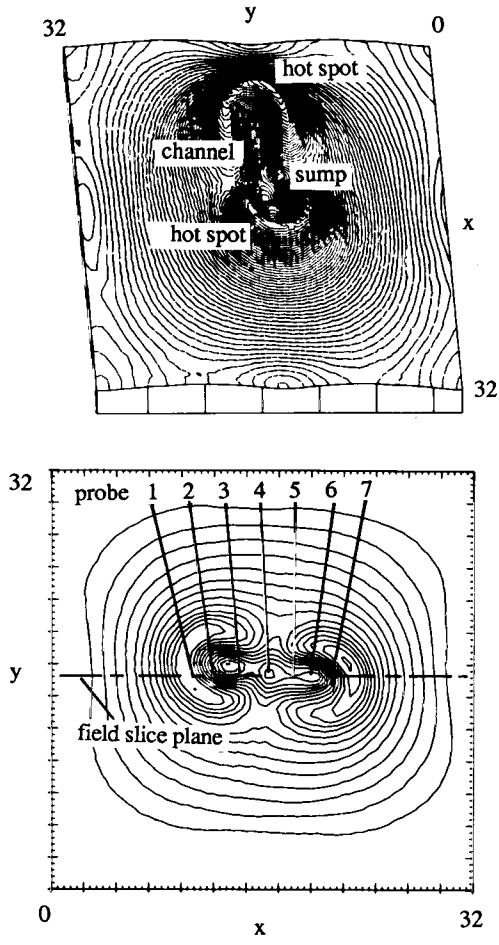

Figure 3.17. Isometric and planar views of self-consistent magnetic fields at $T = 255$ showing elliptical core and one-sided isobaric channel between energy maxima. Peak field squared = 1.5 units, 0.1 units/contour.

250 kA current. Figure 3.18a (t=40 ns) shows that the Bennett relation has been established and the conducting paths are confined to circular (but filamentary) cross-sections. At time$t$=60 ns, the second frame shows that, in addition to the plasma flowing off the filaments, plasma external to the pinches has been compressed into the central core and also into a channel on the right-hand-side of the core. For the parameters of this experiment, $v_{comp} \approx 100$ km / s (10 cm / μs). Figure 3.18b shows the time evolution (of wire midsections) as they explode into Z pinched plasmas. Each filament undergoes about a dozen pinch oscillations the first 40 ns [Felber and Peratt 1980], followed by the appearance of inward "jets" of plasma toward the core. The jets of plasma coalesce

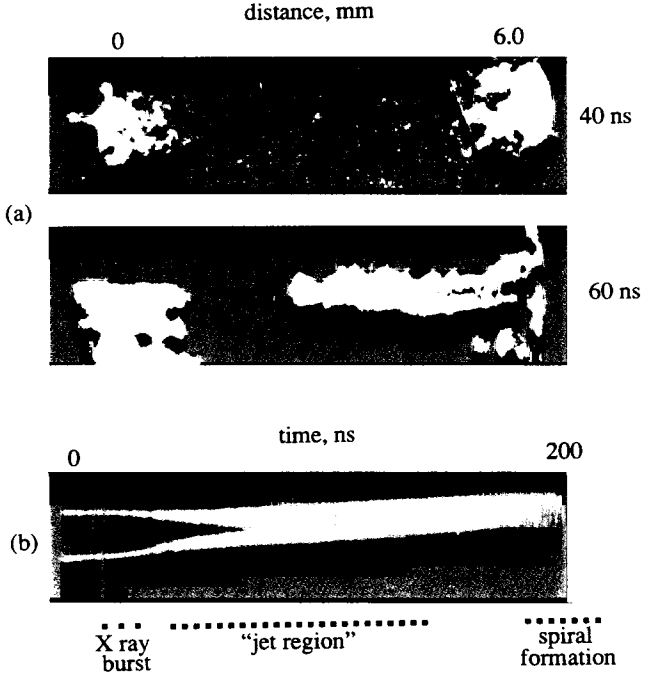

Figure 3.18. (a) Schlieren photographs of plasma light from of two interacting current-carrying plasma filaments (Z pinches) at times 40 and 60 ns, respectively (end view). The pinches are produced by exploding two parallel, 15 mm diameter, stainless steel wires with 250 kA of current. The two space frames show that plasma from the right-hand side filament has been channeled towards the central core, by the magnetic field isobars, at a velocity of about 100 km/s. The process is slightly asymmetrical: Plasma from the right-hand side filament has reached and filled the core at time 60 ns, whereas the plasma from the left-hand side filament has not yet started to move inward. **(b)** Streak camera photograph showing time evolution of interacting Z pinches conducting 667 kA (side view). A slit focused the midsections of the wires onto the film (cf, Figure 6.21). Three distinct regions are recorded: A radiation burst lasting about 5 ns, a "jet" region lasting about 50 ns, where plasma from the exploded wires is channeled *inwards* [as well as change in the circular cross sections (Figure 3.19)] and then, a spiral region, where the filaments rotate about each other. Reference is made to Figure 1.15 for a similiar radiation pattern in astrophysical plasma.

in the core at about 80 ns. However, with regard to radiation in the axial direction: This continues to come from the intense electron currents in two hot spots at the outer locations. This phase is followed by the rotation of the filaments into a spiral structure. A half-rotation is observed to take about 100ns, corresponding to a rotation velocity of about 15 km/s.

The radiation burst is an extremely transient phenomena, lasting for only about 5 ns. This appears to be correlated with the constriction of the single Z pinches to very small diameters, but is intense only when when two Z pinches are present.

3.10.5 Net Motion

The long term motion between the filaments is nonlinear and involves a reconfiguration of their cylindrical cross-sections. This motion is shown in Figure 3.19 for simulation time up to $T = 1{,}700$. As shown, the initially circular cross-sections are deformed into ovals that then take on a "jelly-bean-like" profile prior to forming embryonic spiral arms. Once formed, the arms become thin as they trail out behind the rotating center.[1] Not shown in this sequence is plasma confined in the core, onto which the outer plasmas converge, which tends to obscure the nuclear region.

Since $\mathbf{E} \parallel \mathbf{B}$ is out of the plane of the page, the column electrons spiral downward in counter-clockwise rotation while the column ions spiral upward in clockwise rotation. The current density is $j = n_e q_e v_e + n_i q_i v_i$. A polarization induced charge separation (Section 3.10.3) also occurs in each arm, which, as it thins out, produces a radial electric field across the arm. Because of this field, the arm is susceptable to the diocotron instability (Section 1.7.3). This instability appears as a wave motion in each arm and is barely discernable in the single frame photographs in Figure 3.19 at late times. However, the instability is readily apparent in the spiral rotational velocity curve. Figure 3.20 is the rotational velocity curve for the spiral configuration shown in the last frame of Figure 3.19.

The velocity essentially consists of a linearly increasing component due to a central body undergoing rigid rotation, with two "flat" components on either side of $r = 0$ due to the trailing arms. The diocotron instability modulates the "flat" components at the strong-magnetic-field, low-density instability wavelength Eq.(1.16).

3.10.6 "Doubleness" in Current-Conducting Plasmas

The r^{-1} dependency of the Biot–Savart force law between current-conducting filaments leads to a curious phenomena: a pairing of filaments (c.f. Section 2.6). This pairing leads directly to a "twoness" or "doubleness" when many filaments are present in plasmas in which the magnetic field plays a major role.

As an example, Figure 3.21 shows the evolution of three plasma filaments having parameters identical to those of Section 3.10.1 but spaced $3\Delta'$ and $6\Delta'$ apart. The two closest interact strongly to form a spiral while the third filament remains relatively quiescent. Examples of pairing in the filaments formed in the dense plasma focus (Section 4.6.2) is given by Bernard et al. (1975) and Bostick (1986).

3.11 Magnetic Fields in Cosmic Dimensioned Plasma

3.11.1 Measurement of Galactic Magnetic Fields

Interstellar magnetic fields in spiral galaxies can be observed indirectly in the optical and radio range. In recent years observations of the linearly polarized radio continuum emission led to a significant improvement of the data. Extensive reviews of the observational methods have been published [Heiles 1976, Spoelstra 1977, Verschuur 1979, Sofue et al. 1986] and the results reviewed by Wielebinski (1989). The methods used to measure magnetic fields in galaxies include the following:

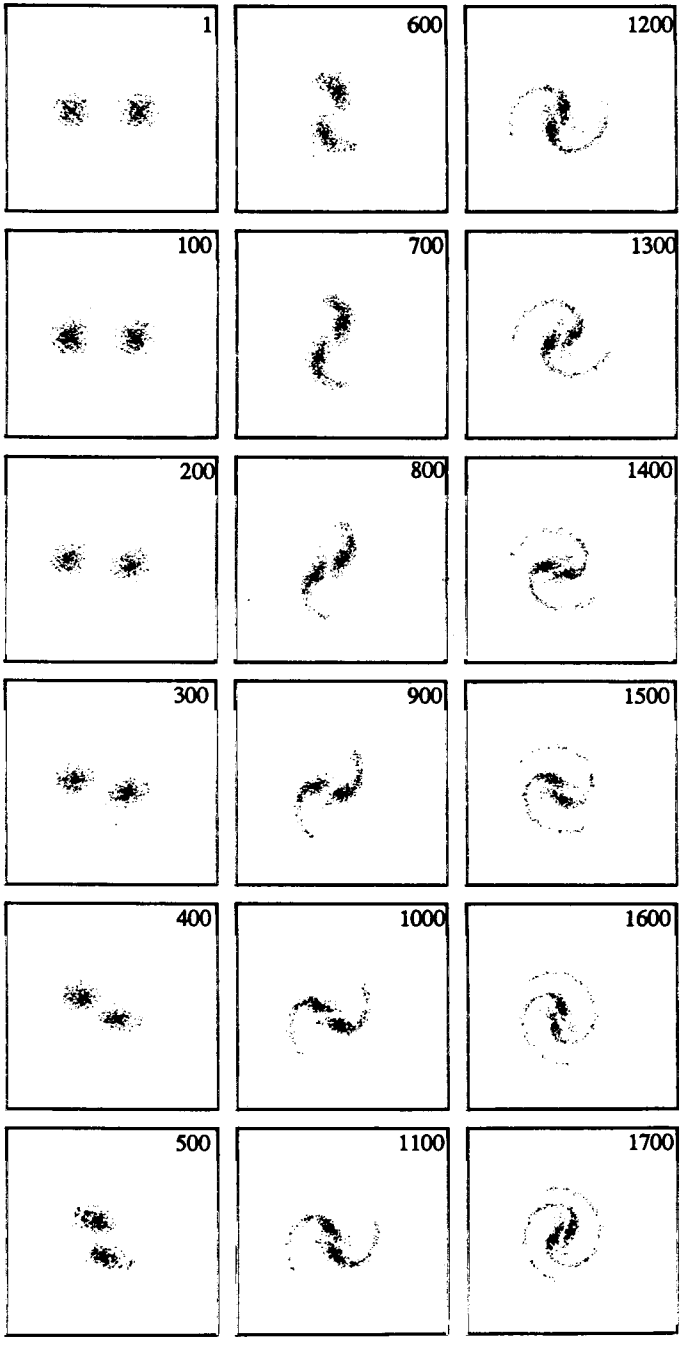

Figure 3.19. Single frame stills of plasma in the simulation of two adjacent Birkeland filaments: $\omega_b / \omega_p = 3.0$, $T_{e0} = T_{i0} = 32$ keV, T = 1–1700, and acceleration field = 62 mV/m. Not shown is the plasma trapped in the elliptical core at the geometric center of the simulation. The plasma tends to obscure the coalesed region.

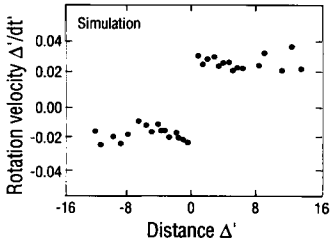

Figure 3.20. Rotational velocity of two adjacent Birkeland filaments. Note the fine scale structure due to the diocotron instability (Section 1.7.3) on the "flat" portions of the velocity curves. The velocity is given in simulation units.

Optical Polarization. Elongated paramagnetic dust particles become oriented perpendicular to the interstellar magnetic field lines by the effect of paramagnetic relaxation, first discussed by Davis and Greenstein (1951). Extensive observations of several thousand stars revealed regular features of the magnetic field in our Galaxy with the distance range of the observed stars. The field strength and the degree of uniformity of the field, however, can only be determined with limited accuracy because too little is known about the size, shape, temperature, and magnetic properties of interstellar grains.

Zeeman Splitting of Radio Lines. Spectral lines are split up when the emitting atoms enter a magnetic field. The amount of splitting in a longitudinal field is 2.8 Hz/μG for the neutral hydrogen (HI) and 3.3 Hz/μG for the OH radio line and has been observed in several Galactic clouds [Verschuur 1979].

Faraday Rotation of Polarized Radio Emission. Continuous radio emission is observed from interstellar plasma clouds (HII regions) which radiate by interaction of thermal particles (free–free emisssion), and/or by synchrotron emission. Thermal radio emission is unpolarized, and synchrotron radiation is partly polarized.

The plane of polarization of a linearly polarized radio wave is rotated when the wave passes through a magnetized plasma according to Eq.(B.14). For an electron plasma, positive (counterclockwise) Faraday rotation occurs if the magnetic field is directed towards the observer; negative (clockwise) Faraday rotation occurs if the field points away from the observer. For a positron plasma, the situation is reversed. From Eq.(B.14), the rotation angle $\Delta\chi$ increases with the integral of $[n_e B_{\parallel}]$ over the line of sight (where $B_{\parallel}$ is the magnetic field component along the line of sight) and with λ^2 (λ = wavelength of observation). The quantity $\Delta\chi / \lambda^2$ is called the "rotation measure" (RM).

An accurate determination of RM requires observations at (at least) three wavelengths because the observed direction of the polarization vectors is ambiguous by $\pm n$ 180°.

Synchrotron Radiation. The average field strength $B_{\perp}$ can be estimated from the average synchrotron intensity Eq.(6.94) since the intensity depends on the field strength and the density of cosmic-ray electrons in the relevant energy range. However, to make this estimation, an equipartition

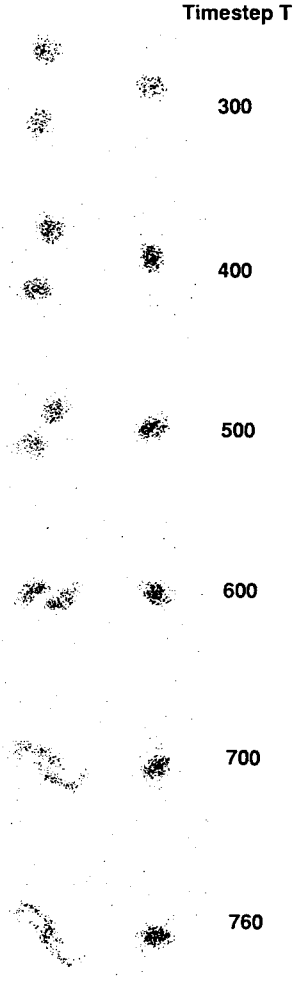

Figure 3.21. Interaction of three Birkeland filaments. Same parameters as Figure 3.19.

between the energy densities or pressure equilibrium of the magnetic field and cosmic rays is assumed. Since the strength of the magnetic field and the local star formation rate are related quantities, equipartition is not valid, and the field strengths estimated are too small [Beck 1990].

3.11.2 Milky Way Galaxy

In the solar neighborhood, the strength of the magnetic field has been determined with rather high accuracy, applying methods in both the optical and the radio range. From the rotation and dispersion

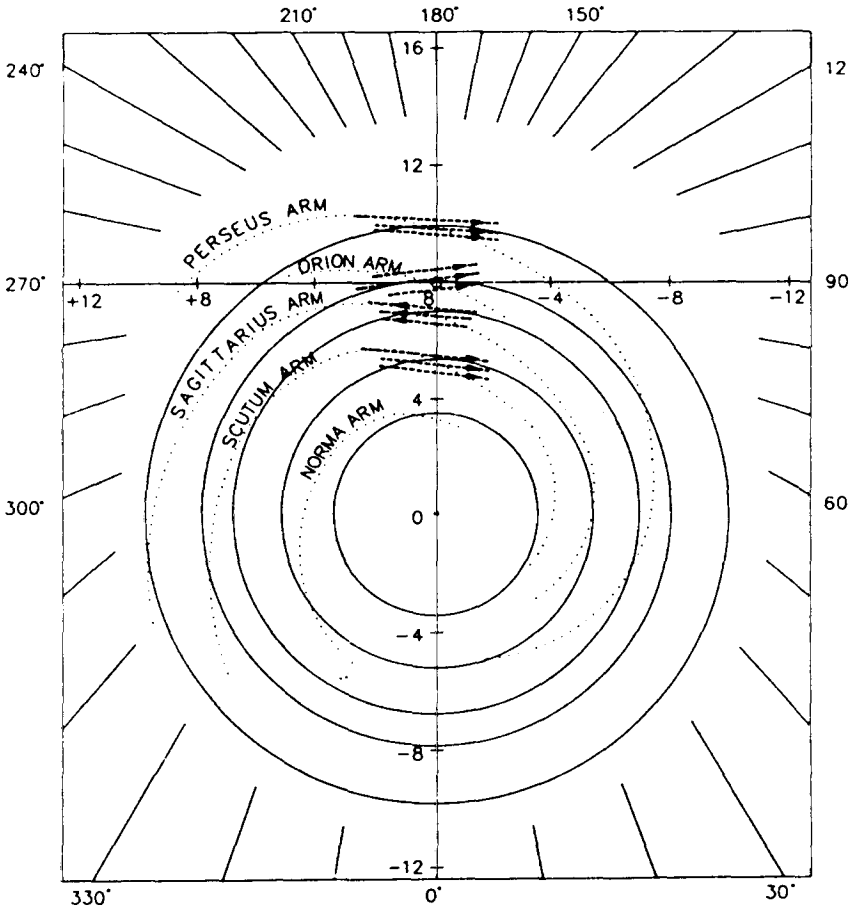

Figure 3.22. Model of the magnetic field in our Galaxy (courtesy of R. Beck).

measures of 38 pulsars within 2 kpc from the sun, the strength of the uniform field has been found to be $|B_\parallel| = 2.2 \pm 0.4$ μG. The total synchrotron radiation radio emission in the anticenter direction yields an effective total field strength of 6 ± 1 μG. A uniform field of 3 μG plus a turbulent field of a similar strength yields a total field strength of ~4 μG which is sufficient to account for the minimum Galactic radio emission between spiral arms, using the local cosmic-ray electron density [Phillips et al. 1981]. The maximum effective field in spiral arms has to be stronger; its strength depends on the clumpiness of the field along the line of sight. If magnetized plasma clouds occupy 5% of the line of sight, the mean strength in the plasma clouds must be ~45 μG.

The observations are roughly consistent with this value. Zeeman splitting of HI lines revealed field strengths up to 50 ± 15 μG in Orion A [Harnett 1984]. The OH lines allow measurements with higher accuracy. In a molecular cloud in NGC 2024 the field stength is $B_{\parallel} = -38 \pm 1$ μG [Crutcher and Kazés 1983]. Faraday rotation of radio waves from background sources reveal field strengths of a few microgauss in HII regions and up to 50 μG in molecular clouds [Heiles, Chu and Troland 1981].

Measurements of the Zeeman effect have now been made in HI clouds [Verschuur 1987], OH molecular clouds [Crutcher et al 1987], and in H_2O masers [Fiebig and Güsten 1988]. These data indicate that the magnetic fields in the Galaxy are along the local spiral arm (i.e., azimuthal). For example, Vallée (1988) shows that any deviations of pitch angle of the field from the spiral arm are slight, possibly less than 6° (Figure 3.22). Valée also deduces a field reversal in the Sagittarius arm. This could support claims that the galactic magnetic field is bisymmetric [Sofue and Fujimoto 1983].

High resolution radio continuum VLA observations at 6 and 20 cm wavelengths [Yusef-Zadeh, Morris, and Chance 1984] reveal numerous plasma filaments in the inner 60 pc (3×10^{18} m or 317 light years) of the Galaxy, ~0.3 pc in diameter by 10–60 pc in length (Figure 1.14). The filaments are highly polarized, indicating a synchrotron origin for the radio emission. The filaments are aligned roughly perpendicular to the galactic plane so that the magnetic field is poloidal in a cylindrically force-free configuration. The polarization structure near the Galactic center has been recorded with the Effelsberg 100 m telescope by Seiradakis et al. (1985) at 6.3 cm (4.75 GHz) and 2.8 cm (10.7 GHz). Figure 3.23 shows a radiograph of the intensity of polarized emission at 10.7

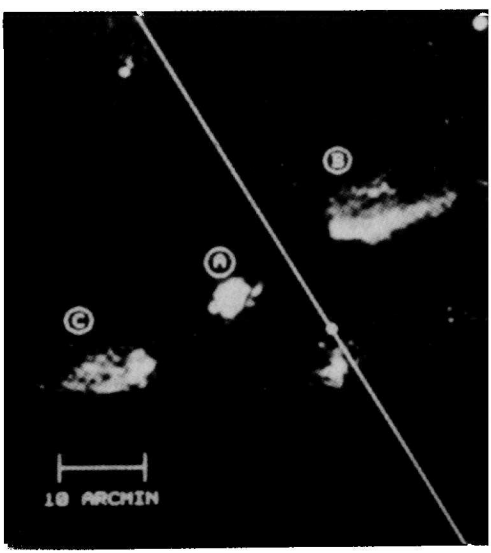

Figure 3.23. Polarized intensity radiograph (linear scale) of Galactic center at 10.7 GHz. The peak polarized flux density of components A, B and C is 690, 310, and 140 mJy, respectively (courtesy of R. Beck).

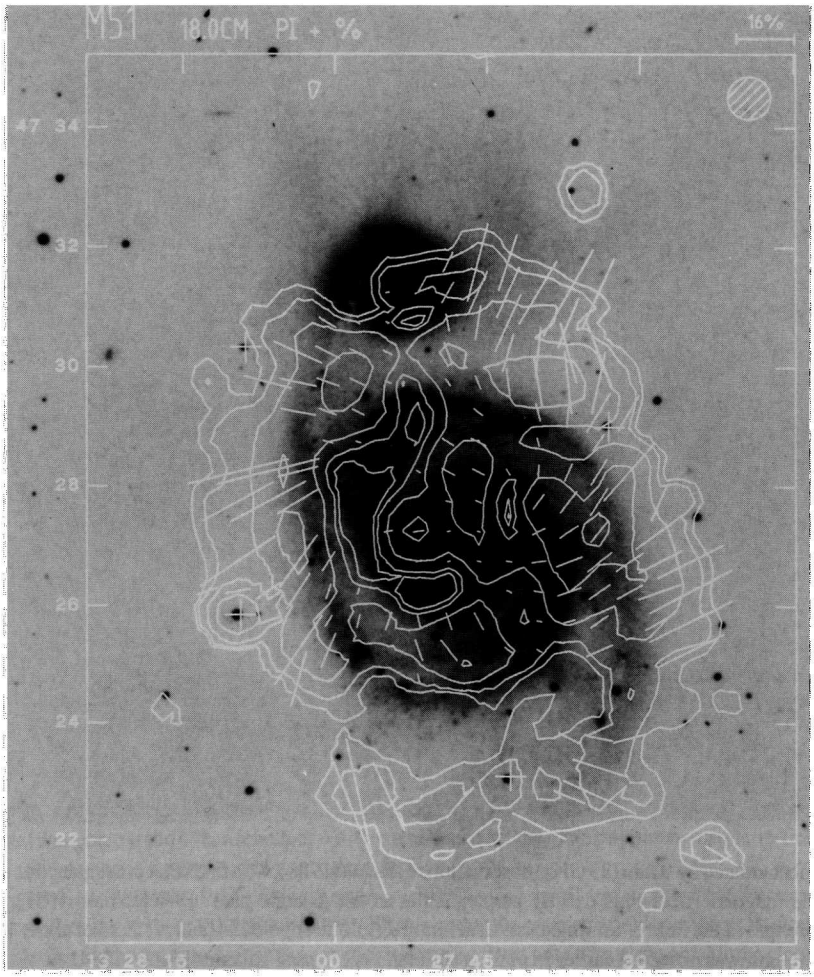

Figure 3.24. Bisymmetric spiral structure in the linearly polarized radio emission from spiral galaxies. **(above)** Flux density of M51 at 1.66 GHz (18.0 cm). The sensitivity is 30 mJy per beam area **(p. 126)** Flux density of the linearly polarized emission of NGC 6946 at 4.75 GHz (6.3 cm) superimposed on an optical photograph. Contours are drawn at 0, 1, ..., 5 mJy/beam area. The lengths of the **E** vectors are proportional to the degree of linear polarization. The ellipses indicate radial distances of 6 and 12 kpc (courtesy of R. Beck).

GHz and depicts two radio lobes on either side of a core. Seiradakis et al. note that the "core-lobe" structure is the same as that of a classical double radio source. Seiradakis's results have been

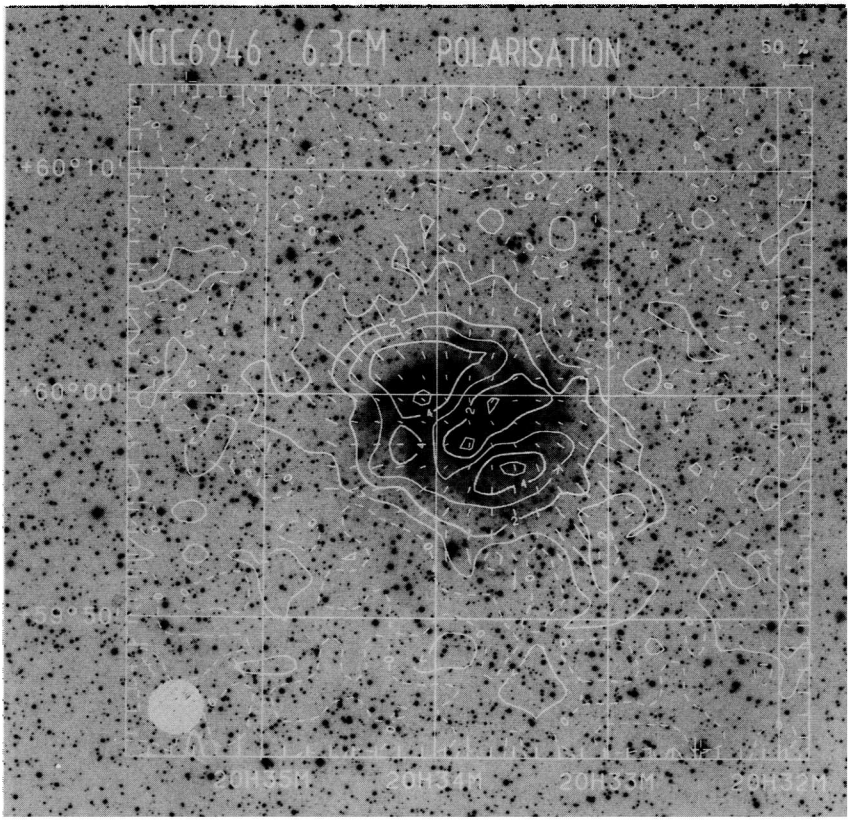

substantiated by 9 mm (33 GHz) observations of Reich (1988), who finds that in the galactic center the magnetic field runs exactly perpendicular to the galactic plane [Wielebinski 1989]. The strength of the field is 1 milligauss. An azimuthal (toroidal)/poloidal galactic field of about 1 mG strength was observed earlier in plasma simulations of spiral galaxies [Peratt 1984].

3.11.3 Spiral Galaxies

During the last decade, radio polarization observations have revealed large-scale magnetic fields in spiral galaxies. For example, the Effelsberg radio telescope has collected polarization data from about a dozen spiral galaxies at 6 to 49 cm wavelengths [Beck 1990]. Rotation measures show two different large-scale structures of the interstellar fields: Axisymmetric-spiral and bisymmetric-spiral patterns [Krause 1989]. Figure 3.24 illustrates two cases of bisymmetric spiral structure in the large-scale magnetic field of spiral galaxies [Harnett et al. 1989, Horellou et al. 1990].

The orientation of the field lines is mostly along the optical spiral arms. However, the uniform field is often strongest outside the optical spiral arms. In IC 342 two filamentary structures are visible in the map of polarized intensity (Figure 3.25). Their degree of polarization of ~30 percent

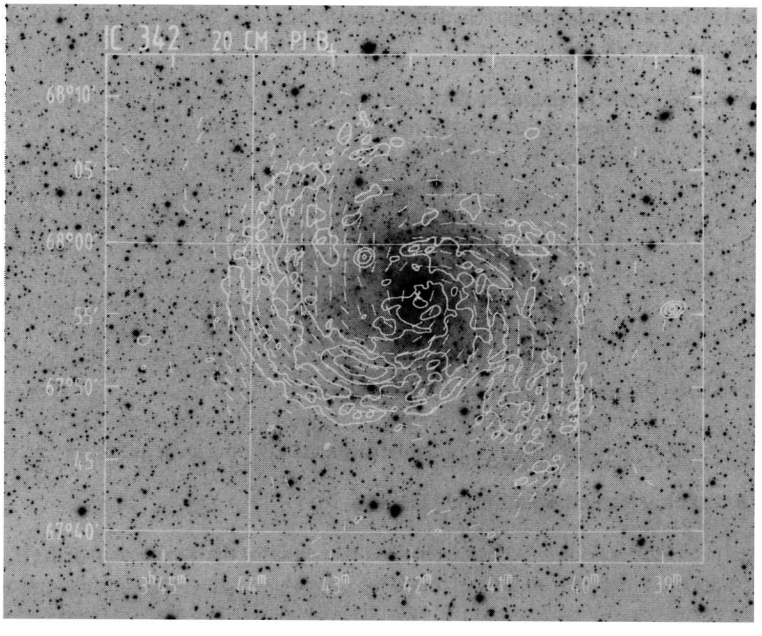

Figure 3.25. Orientation of the observed **B** vectors in IC 342 with an angular resolution of 2.'45, corrected for Faraday rotation as derived from data at 6.3 and 20 cm. The vectors have arbitrary lengths and are superimposed onto a contour map of the linearly polarized intensity at 20 cm (courtesy of R. Beck).

indicates a high degree of uniformity of the magnetic field on the scale of the resolution (~700 pc). These filaments extend over a length of ~30 kpc and hence are the most prominent magnetic-field features detected in normal spiral galaxies so far.

A detailed analysis of the rotation measure distribution in a spiral arm southwest of the center of the Andromeda galaxy M31 [Beck et al. 1990] shows that the magnetic field and a huge HI cloud complex are anchored together. The magnetic field then inflates out of the plane outside the cloud. The tendency for the magnetic field to follow the HI distribution has been noted in several recent observations. Circumstantial evidence has accumulated which suggests that there is a close connection between rings of CO and H_α seen rotating in some galaxies and the magnetic fields in the nuclear regions. This is particularly apparent in observations of spiral galaxies viewed edge-on. This scenario has also been invoked for our Galaxy [Wielebinski 1989].

Neutral hydrogen is detected from galaxies via the van de Hulst radio-emission line at 21.11 cm (1.420 GHz), which arises from the transisition between the hyperfine-structure sublevels of the ground state of a hydrogen atom [Kaplan and Pikelner 1970]. This is the sole procedure for the direct observation of neutral hydrogen in galaxies. High-resolution observation of neutral hydrogen in irregular and spiral galaxies usually reveal extended HI distributions. Contour maps of the HI typically show a relative lack of HI in the cores of spiral galaxies but high HI content in the surrounding region, usually in the shape of a "horseshoe" [Rogstad et al. 1974, Bosma et al. 1977; 1981, Hummel and Bosma 1982, Van Woerden et al. 1983]. This region is not uniform but

may have two or more peaks in neutral hydrogen content. Figure 3.26 shows several examples of HI distributions in spiral galaxies.

Example 3.2 Bisymmetric magnetic field distribution in a simulated spiral galaxy. For the simulated galaxy we choose $\Delta' = 1.66 \times 10^{20}$ m, $dt' = 5.87 \times 10^{11}$ s, a mass per unit length of 10^{41} kg/10^{21} m (10^{44} g/35 kpc), and $B_\phi = 2.5 \times 10^{-8}$ T (c.f., Example 6.3, Section 6.7.2). Figure 3.27 shows the plasma spiral formed in this simulation overlayed on its magnetic field line (squared) isobars. The diameter of the spiral is about 50 kpc with a mass of 10^{41} kg, i.e., a size and mass of that observed from spiral galaxies. A direct comparison to observations is made by superimposing the HI distribution in NGC 4151 on its optical photograph [Figure 3.27b]. The observation shows two peaks in neutral hydrogen surrounding a void. The void is orientated towards one of the arms. The simulation allows the two peaks to be traced back to their origin. Both are found to be the remnants of the originally extended components (i.e., cross-sections of the original Birkeland filaments). As discussed in Section 4.6.3, the accumulation and neutralization of hydrogenic plasma is expected in strong magnetic field regions. The hydrogen deficient center is the remnant of an elliptical galaxy formed midway between the filaments, in the magnetic null (Section 3.11.4).

3.11.4 Rotational Velocities of Spiral Galaxies

Rotational velocities of spiral galaxies are obtained by measuring the doppler shift of the H_α line emitted by neutral hydrogen in the spiral arms. If the galaxy is canted toward earth, the emission-line in the arm moving away from earth is red-shifted while the line in the arm moving towards earth is blue-shifted. Figure 3.28 shows six radial velocity versus radius curves typical of spiral galaxies. These data show 1) a nearly linear solid-body rotation for the galaxy center (the first few arcminutes from center), 2) a nearly radially independent velocity profile in the spiral arms, and 3) distinct structure in the spiral arms that appears on the so-called flat portion of the velocity curve (beyond the first few arcminutes or, equivalently, the first few kiloparsecs).

Example 3.3 Rotational velocity of a simulated spiral galaxy. Using the scaling of Example 3.2, the rotational velocity given in Figure 3.20 can be converted to physical units. The average velocity for the flat portion of the curve is $v = 0.0213\ \Delta' / dt'$, or, in time-compressed units, 6×10^3 km/s. Applying the mass correction factor 10.7 (Section 8.6.3) and the electric field correction factor 2.5,[2] the rotational velocity is 226 km/s. This curve is replotted in the last frame of Figure 3.28 and is in good agreement with the observations. Concomitant with the lengthening of the arms is a thinning of the arms as shown in Figure 3.19. As discussed in Section 3.10.5, a diocotron instability is produced. This instability shows up in both the cross-sectional views of the spiral arms and in the velocity profile, where a distinct vortex "saw-tooth" pattern is measured. Good examples of this instability are found in the Sc-type galaxies M101, NGC 253, and NGC 2998 [Arp 1986]. Figure 3.29, NGC 3646, is an example of a very large diocotron instability, similar to that observed in auroras, in the spiral arms.

Figure 3.26. (opposite) HI distributions superimposed on optical photographs of galaxies. (left column) NGC 4736, NGC 5033, and NGC 4151. (right column) NGC 3198 and M83 [Peratt 1986].

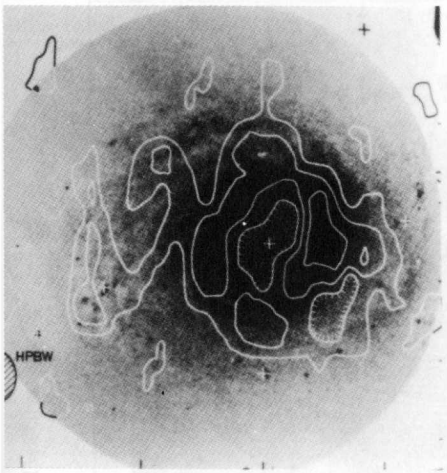
HPBW

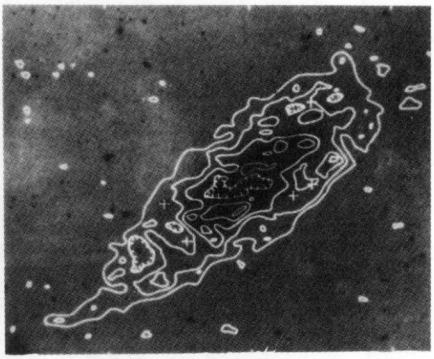

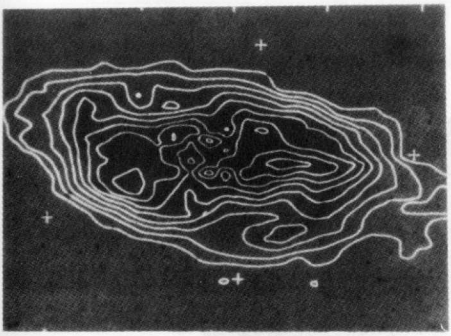

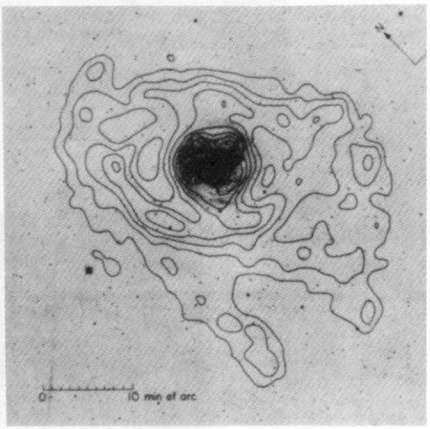
0
10 min of arc

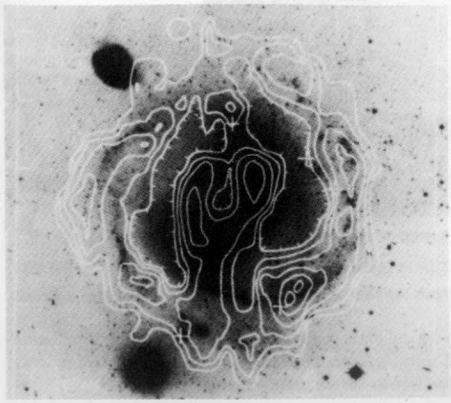

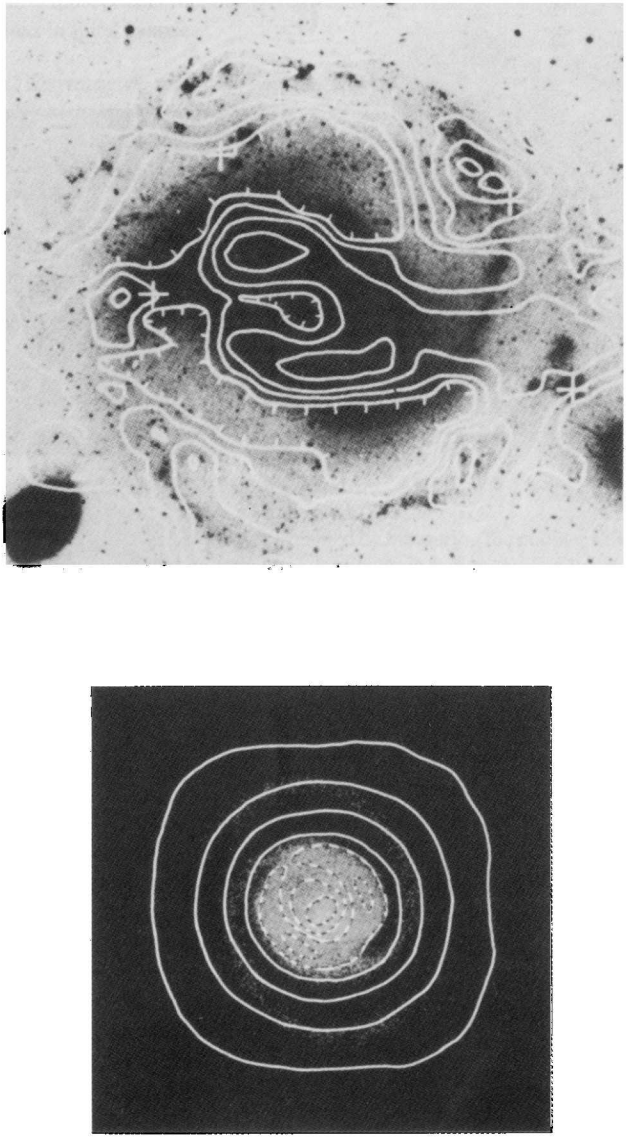

Figure 3.27. (top) HI distribution superimposed on an optical photograph of NGC 4151. **(bottom)** Simulation magnetic energy density superimposed on simulated spiral galaxy. The resolution of the magnetic energy density is insufficient to resolve the magnetic field structure in the simulation spiral arms.

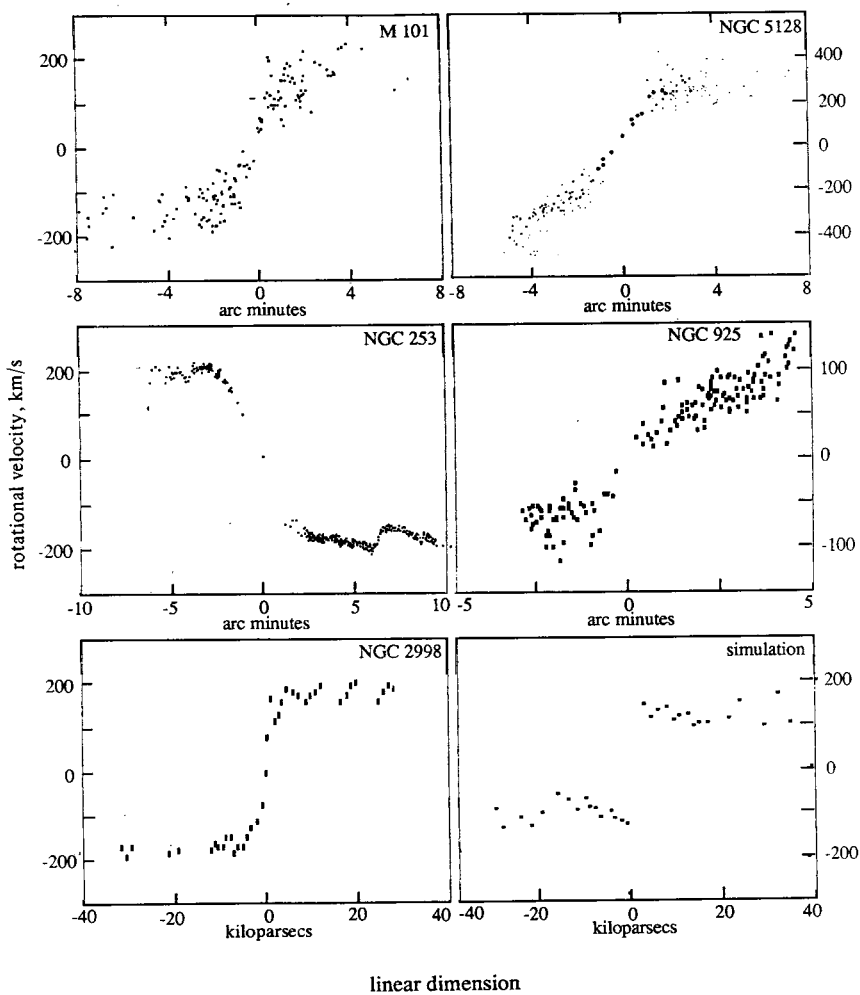

Figure 3.28. Spiral galaxy rotational velocity characteristics. The bottom right-hand-side curve is the simulation result taken from Figure 3.20.

3.11.5 Elliptical Galaxies

Elliptical (E) galaxies, as distinct from peculiars, irregulars, and spirals, are characterized by a very smooth texture, a bright nucleus, and a tenuous outer envelope of large extent (sensitive photographic plates show that the visible envelope may be 20 times the diameter of the nucleus, Figure 3.30).

Ellipticals are most often found midway between the extended radio components of double radio galaxies and radioquasars. Figure 3.31 is an example of this geometry. Like S0 galaxies

Figure 3.29. Optical photograph of NGC 3646. Note the well-defined diocotron instability in the spiral's arm.

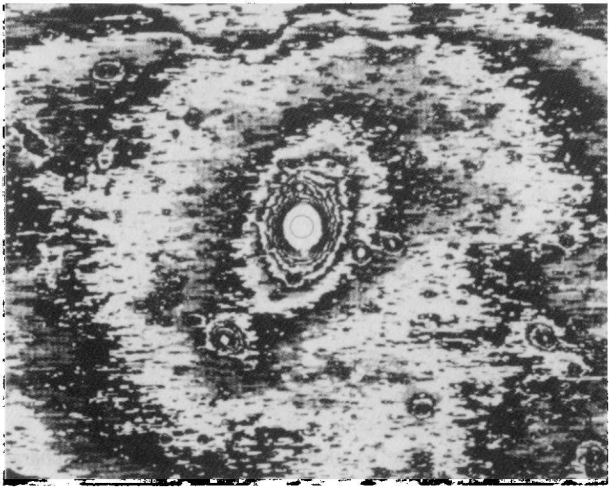

Figure 3.30. Isodensitometer tracing of the elliptical galaxy M87, made from a 60 min exposure with the 1.2 m Palomar Schmidt telescope. The inner circle is the diameter given in the Shapely–Ames catalogue, while the outer ellipse spans as much as 70 arcmin. The horizontal extent of the image frame is 500 arcmin. Note that the inner isophotes have vertical major axes, but the outer isophotes show noticeable clockwise twisting.

Figure 3.31. **(a)** Optical photographs of the elliptical galaxy NGC 1316 and the spiral galaxy NGC 1317. **(b)** Radio and optical structure of NGC 1316.

(galaxies with little or no evidence of star-forming activity) E galaxies are found most frequently in regions characterized by high galaxy density (i.e., areas most susceptible to *interactions*).

Diffuse elliptical galaxies are also found midway between the synchrotron emitting galactic simulation filaments. These galaxies are characterized by a twisting of their outer isophotes. Elliptical galaxies have weak or no magnetic fields.

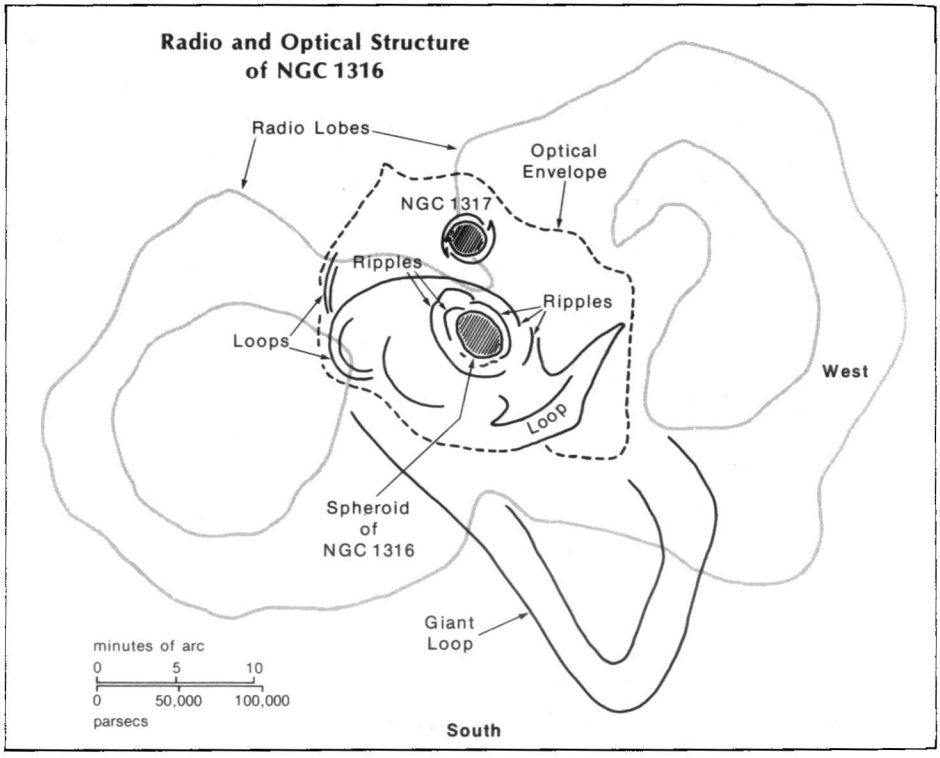

Figure 3.31. (b).

Example 3.4 Simulated elliptical galaxy. Figures 3.15 and 3.17 depict the elliptical core formed in a plasma galaxy simulation. In physical units, the bottom frame of Figure 3.16 corresponds to an elapsed time of 20 Myr from the start of the filament interaction. At this time, the field strength squared in the vicinity of the core (approximately midway up the figure) is $B_\phi = 0.592 \times 10^{-8}$ T. The field induced pressure defining the boundary of the core at this time is $p_B = (2\mu_0)^{-1} B_\phi^2 = 1.4 \times 10^{-11}$ Pa (1.4×10^{-10} dyn/cm^2). This isobar extends some 50 kpc and can balance the thermokinetic pressure of a 10^4 m^{-3} (10^{-2} cm^{-3}) 6 keV plasma compressed into the core. The magnetic field is null at the core center.

As is the case with elliptical galaxies, the simulated elliptical plasma galaxy shows only a slight twist of rotation (Figure 3.17), caused by the start of a clockwise rotation of filaments beginning a Biot–Savart force law interaction (Section 3.10.3).

3.11.6 Intergalactic Magnetic Fields

A large-scale intercluster magnetic field with an estimated strength of 0.3–0.6 μG located between the Coma cluster of galaxies and the Abell 1367 cluster was discovered in 1989 [Kim, Kronberg, Giovannini, and Venturi 1989] (Section 2.6.6).

Notes

[1] Bostick (1957) was the first to observe the formation of spiral structures produced by interacting plasmoids crossing magnetic field lines.

[2] To reduce the computation time to spiral formation, the acceleration field E_z was increased 2.5 times, from 12 mV/m to 30 mV/m. A field strength ~ 1–10 mV/m is consistent with that associated with double layers in the near-earth plasma (Section 4.4). It should be noted that over the axial extent of a spiral galaxy, ~ 10 kpc, a millivolt per meter field strength corresponds to a potential of 3×10^{17} V (Section 5.6.4).